Ref. Ares(2023)8399098 - 07/12/2023

This project has received funding from the European Union's Horizon 2020 research and innovation programme under grant agreement No 964644

Gamma MRI

Grant Agreement number: 964644
Project acronym: GAMMA-MRI
Project title: Gamma-MRI: the future of molecular imaging
Funding Scheme: H2020-FETOPEN-2018-2019-2020-01

Deliverable 5.1

Report on biophysical model

PROJECT START DATE: 01/04/21

Deliverable nature:	Report
Dissemination level:	Public
WP number	5
Due date	31.09.2023
Submission date	04.12.2023

Contribution list

Prepared by	Renaud Jolivet (UM)	24.11.2023
Reviewed by	Luis Fraile (UCM)	25.11.2023
Reviewed by	Tomás Rodriguez (Inspiralia)	24.11.2023
Approved by	Stavroula Pallada (HESSO)	07.12.2023

Distribution list

Internal		**External**	
Consortium partners	Y	European Commission	Y
		External Advisory Board	N

Table of versions

Author	**Version**	**Date**	**Description**
Renaud Jolivet	V1.0	24/11/2023	1st draft
Renaud Jolivet	V2.0	28/11/2023	Revised version

To Be Cited As

D5.1 “Report on biophysical model” of the Horizon 2020 project GAMMA-MRI, EC Grant Agreement No. 964644

Disclaimer

This document reports on the activity related to the GAMMA-MRI according to the Grant Agreement No 964644. It reflects only the author's view. The European Commission is not responsible for any use that may be made of the information it contains.

Table of content

List of figures

List of tables

NA

List of annexes

Annex 1: Parameters and equations of the original model under study

List of abbreviations

NA

1. Introduction

1.1. Purpose of the document

WP5 aims at producing the first proof-of-concept brain image of a rodent brain using the low-field GAMMA-MRI prototype via delivery of polarised metastable xenon. The work package also contains support activities designed to explore various *ad hoc* solutions and questions, looking at the final goal of the project from a more biological angle than the rest of the GAMMA-MRI consortium. One of these *ad hoc* activities is the use of computational models based in biophysics and biochemistry, to assess what kind of biological information might be within reach over the long-term development of the GAMMA-MRI imaging modality.

Specifically, we set out to adapt a recently developed mathematical model of intercellular interactions, linking PET and fMRI signals to the underlying brain physiology, to GAMMA-MRI, focussing on interactions between xenon and brain physiology, and providing a detailed understanding and qualitative predictions of the biological mechanisms underlying the signals to be collected *in vivo*.

Since the beginning of the project, with efforts for now focussed in the second reporting period, we analysed a computational model of brain energy metabolism using a new approach (for computational biology) to try to understand what biological processes influence the generation of signals from various brain imaging modalities, and how this would influence the kind of biological information that can be assessed using the new modality prototyped by the GAMMA-MRI consortium. We also expanded our computational framework in two new directions that are discussed below.

In this report, we aim to describe the result of these efforts, the initial conclusions that we have reached, and discuss future work.

2. Biophysical modelling of GAMMA-MRI signals

2.1. Modelling neuron-astrocyte-vasculature interactions and their links to brain imaging modalities

Computational modelling of brain activity has been for decades heavily focussed on neurons and neural networks. This narrative is pervasive in the cognitive and systems neuroscience communities, where clinical functional brain imaging methods such as positron emission tomography (PET) and blood oxygen-level-dependent functional magnetic resonance imaging (BOLD fMRI) are used to infer localised neuronal activity, and how different brain areas communicate which each other. This is an issue, because the brain consists of a large proportion of non-neuronal (glial) cells, and these cells play a key role in shaping the signals detected by these modalities. As a matter of fact, both BOLD fMRI and PET, and probably soon GAMMA-MRI, detect mostly metabolic proxies of neuronal activity, rather than neuronal activity itself. (We are aware of course that both PET and MRI can be used to measure many other things about the brain. However, we would argue that GAMMA-MRI as it stands, most resembles those specific modalities that measure vasculature-related biological signals.)

In practice, this imposes a limitation on the spatial and temporal resolutions at which biological processes can be sampled. This is because any tissue activation leads to the recruitment of blood vessels distant from the activation locus, thus limiting the spatial localisation of the underlying neuronal signals. Additionally, the recruitment of metabolic processes in non-neuronal cells, which have typical timescales far slower than those of neuronal electrophysiological processes, limits the temporal resolution with which any modality can probe neuronal activity via these proxies. We believe, however, that this offers an interesting opportunity to the GAMMA-MRI prototype (and imaging modality), depending on how fast image acquisition can be performed.

To investigate these questions, we proceeded to implement a relatively novel computational analysis method called Computational Singular Perturbation to the model of neuron-astrocyte-vasculature metabolic interactions, which we have developed and validated in our lab over the years.

2.2. Reimplementation and validation

First, to proceed with the application of CSP to our model and use pre-existing packages, we needed to reimplement the model from its original MATLAB implementation. This was also technically necessary to separate reactions originally formulated in MATLAB as bidirectional reactions into separate reactions. The overall structure of the model can be seen in Figure 1below.

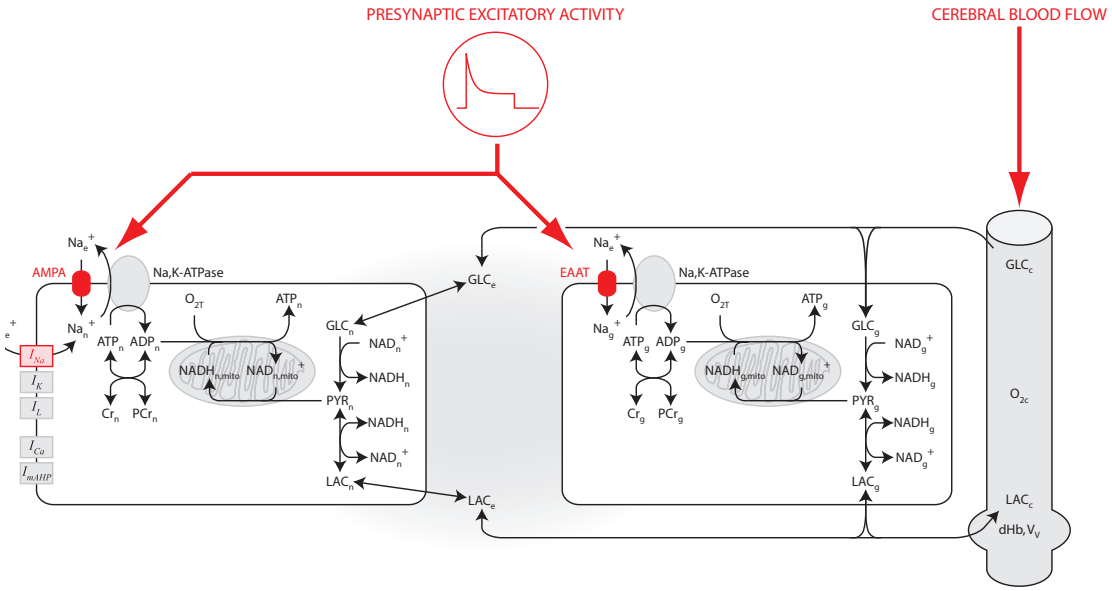

Figure 1. Model of neuron-astrocyte-vasculature metabolic pathways (adapted from Jolivet et al., PLOS Comput. Biol., 2015 for illustrative purposes).

Broadly speaking, the model simulates the essential metabolic interactions between neurons (left box), glial cells (middle box) and the vasculature (red box), as well as exchanges between them via the parenchyma, and the key metabolic processes activated in neurons in direct connection to incoming presynaptic electrophysiological activity. Because of small adaptations to the model since its publication and because of its reimplementation in a new mathematical formulation, the first step consisted in validating this new implementation before we could proceed with further analysis. Figure 2 below details the results obtained while simulating the model in a typical human activation scenario (grey area), as detailed in the original version of the model.

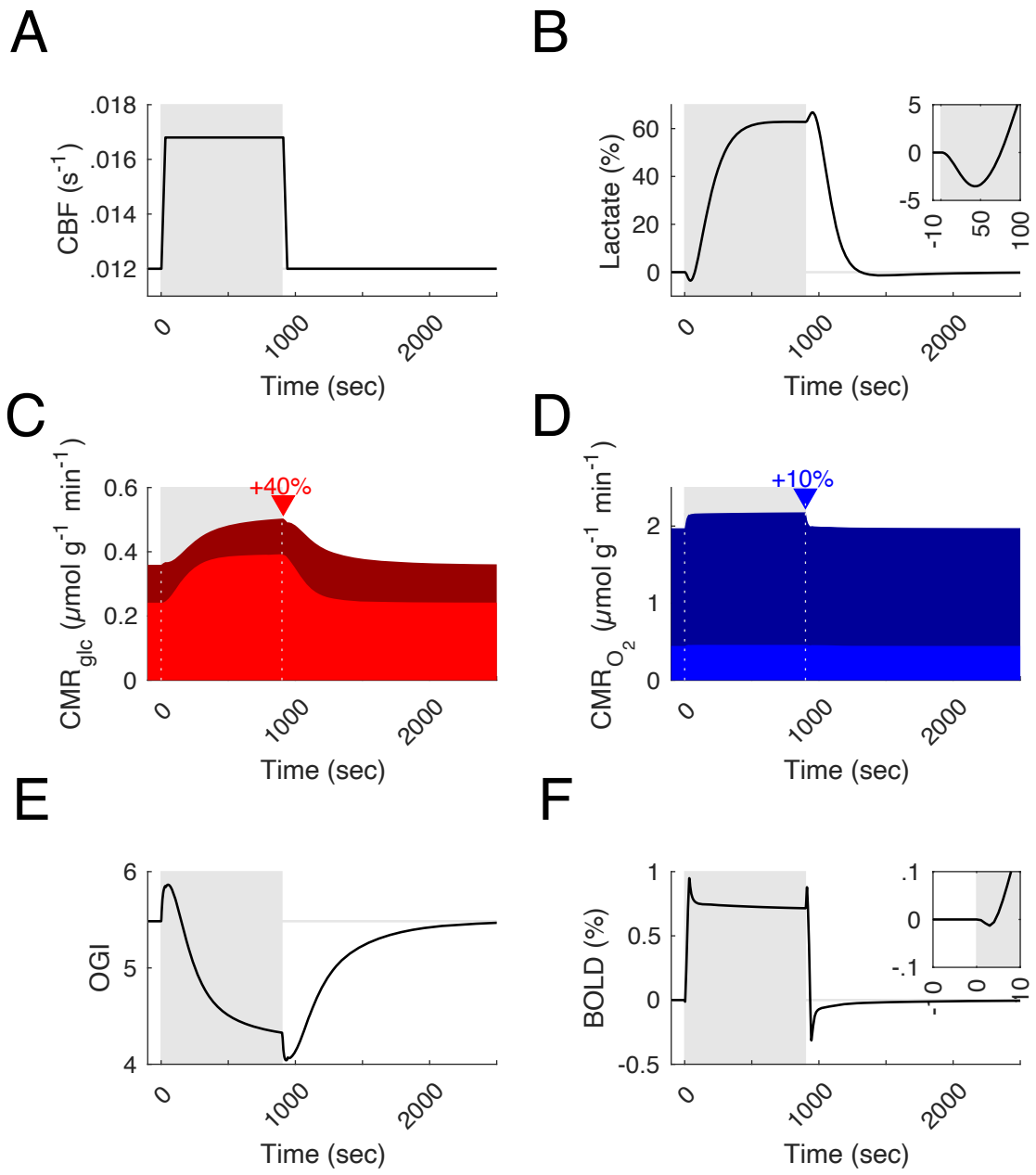

Figure 2. Reproduction of the key results for a simulation of human metabolic activity following a sustained period of activation (adapted from Jolivet et al., PLOS Comput. Biol., 2015 for illustrative purposes).

These results demonstrated that the new implementation reproduced the original results. They also illustrate the power of the model in making accurate qualitative – and to some extent quantitative – predictions about the time course of key metabolic variables following activation, such as the relative brain uptake of oxygen (Figure 2D) and glucose (Figure 2C), the ratio of oxygen to glucose consumption (Figure 2E), and the dynamics of the key metabolic by-product lactate (Figure 2B). They also illustrate the capacity of the model to make predictions about the time course of the BOLD fMRI signal that would be collected from a corresponding voxel (Figure 2F). It is important to note that none of these results were originally built in the model.

2.3. Computational Singular Perturbation (CSP)

We then proceeded to apply CSP to the model. The model of brain energy metabolism considered here can be simulated in several scenarios, but we focussed exclusively on *in vivo* human brain activation, which is most relevant long-term for GAMMA-MRI. The simulations contain two epochs of interest: (i) the activation epoch (from 0 to 900 s; see Figure 2), when external input to the cortex drives neuronal activity and subsequently brain energy metabolism, and (ii) the post-activation epoch (from 900 s), after external input to the cortex is over, but brain energy metabolism is still recovering, owing to its naturally slower dynamics.

It is sufficient here to say that the CSP methodology outputs several indicators and diagnostics that allow investigating in detail the behaviour of the model. Given a set of ordinary differential equations, CSP classifies the modes – the sum of which determines the evolution of the system – in two categories: (a) exhausted modes characterized by fast timescales that generate equilibria in the phase-space within which the system evolves, and (b) active modes characterized by slow timescales that drive the system within the established equilibria. This classification, meaningful when a wide range of timescales develop in complex networks of biochemical and metabolic reactions such as those found in brain energy metabolism, allows for the development of several algorithmic tools providing system-level understanding. These tools identify (a) the reactions responsible for generating the fast and slow timescales, the latter characterizing the dynamics of the system, (b) the reactions contributing to the formation of equilibria, (c) the fast variables (metabolite concentrations) slaved to the remaining ones via established equilibria, and (d) the reactions and metabolic species that control the slow evolution of the system via the active modes.

Figure 3 shows a cartoon drawn for illustrative purposes of what the timescales identified by CSP can look like in a study like ours. The approach algorithmically defines the periods in which the number of exhausted modes is constant, denoted by blue arrows in Figure 3. During a specific period, the timescales below the blue arrow are those that characterize the development of equilibria, as the fast modes become exhausted, while the timescales standing above the blue arrow relate to the active modes that govern the system's evolution. In each period, the characteristic timescale is related to the active mode that has the largest impact in driving the process, i.e. the fastest of the non-exhausted modes. Another way to think about this approach is as an algorithmically-driven separation of timescales, a method that is commonly used in computational biology to simplify the dynamics of complex systems modelled as series of coupled ordinary differential equations.

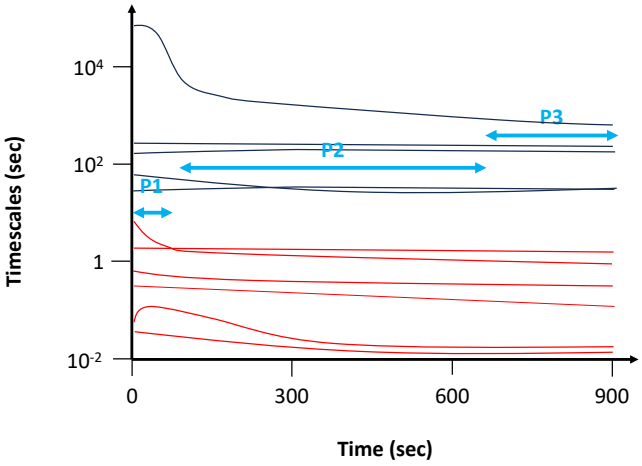

Figure 3. CSP allows for the automated algorithmic segmentation of model behavior in various key periods. In each period, the key biological mechanisms that drive the behavior of the set of reactions can then be identified.

While the tool is very powerful, in practice, due to the relative complexity of metabolic networks, it does not necessarily outputs modes that can be neatly and simply mapped to one specific biological process. Instead, the active slow mode that dominates the system's slow evolution usually consists of a mixture of a few dominant metabolic reactions and metabolites, that then needed to be carefully interpreted in their relevant biological context to yield meaningful biological information.

We programmed a tool to visualise the network in Figure 1 identifying exhausted reactions and the contribution of various metabolites in various periods (not shown), but it is our opinion that due to the complex nature of the underlying biology, and of the analytical method applied here, these visualisations are in the end of limited use.

2.4. Analysis and importance for the GAMMA-MRI modality

Beyond the interest we have in understanding better the dynamics of the biological system that underpins our model, the CSP extracts important findings and has implications for GAMMA-MRI.

2.4.1. General considerations

Our analysis suggests that most of the equilibria in the activation epoch are established in period 1 (P1), few more are added in P2 and one more in P3 (periods 1, 2 and 3 cover the entire activation period). In period 1, the established equilibria involve a larger number of reactions in the neuronal compartment than in the glial compartment. This points to two conclusions.

First, it suggests that persistent presynaptic activation to a brain region very rapidly drives the local metabolic network from its baseline steady-state to an alternate activated steady-state. Second, it suggests that this transition is mostly complete within the initial period 1, which lasts about 1 min. We found that most of the fast modes in period 1 have an associated timescale below 1 s, with only four of them having a timescale slightly above 1 s (but less than 2 s). To put this in perspective, the longitudinal relaxation times measured for xenon isotopes

in the biological environment vary from T_1 = 5.6 ms in pure water at 298°K for ^{131}Xe (Stengle *et al.*, *J. Phys. Chem. A* 88, 1984), to a T_1 for ^{129}Xe between 3.6 s (B_0 = 2.35 T) and 26.0 s (B_0 = 4.7 T), measured in the brain tissue of a rat in *in vivo* conditions (Shepelytskyi *et al.*, *Magn. Reson. Med.* 88, 2022). We argue that this is a crucial fact for the interpretation of functional data related to brain energy metabolism. In particular, the reactions involving oxygen consumption and transport (from the vasculature to the parenchyma and cells, i.e. reactions A.36, A.39 and A.40 in Table 2 in the annex) exhibit a significant participation in the equilibria that are established in period 1, which lasts up to period 3, while they do not significantly contribute to the slow dynamics of the system. Similarly, transport of lactate from the vasculature to cells and parenchyma (reactions A.34 in Table 2 in the annex), as well as lactate to pyruvate conversion (or vice-versa; reactions A.33 in Table 2 in the annex), all exhibit a similar response, with the notable exception of direct lactate transport between the glial and vascular compartments. Additionally, reactions comprising the glycolysis in both the neuronal and glial compartments (reactions A.30 to A.32) significantly participate in the equilibria that are formed early on in period 1. By contrast, the Na,K-ATPase (A.28), which is responsible for a large fraction of the brain's energy budget and is the main driver of metabolic activation following presynaptic activity (see Harris *et al.*, *Neuron* 75, 2012, for a review), provides a significant contribution to the equilibria in the second period. This is however expected, owing to the relatively slow time constant for sodium extraction (in the tens of seconds).

Concretely, CSP revealed three key findings: [a] the rapid (within seconds) equilibrating of reactions associated with neuronal postsynaptic activity, [b] in response to presynaptic input specifically, a key role for glial oxidative and glycolytic metabolism in driving the observable behaviour of the system following the onset, or offset (not discussed here), of activation, and finally, [c] a role for the creatine phosphate shuttle in late stages of activation and post-activation (again not discussed here). The first two points above are consistent with experimental findings that the BOLD signal observed in fMRI is more correlated to the input to an activated area than with local neuronal activity. Our results are also consistent with experimental findings in positron emission tomography (PET), that metabolic responses upon activation, in particular tissue glucose uptake, are driven by astroglial glutamate transport (Zimmer *et al., Nat. Neurosci.* 20, 2017). Our results, taken with these experimental findings, highlight the need for a re-evaluation of the role of astrocytes in brain clinical imaging signals like BOLD fMRI and [^{18}F]FDG PET (which measures the accumulation of a glucose analogue in activated tissues). Far from the common interpretation that these signals measure local neuronal activity, the results mentioned above, suggest that they instead measure the amplitude of the synaptic input to an activated region and that they are mostly glial in nature.

2.4.2. Considerations for GAMMA-MRI

Our analysis has significant implications for GAMMA-MRI. In the context described above, one of the central limitations of competing imaging modalities like BOLD fMRI or PET, is their low temporal resolution in comparison to the processes they pertain to measure when speaking about neural activity, and this despite continuous advances in the field (less so we are aware for fMRI). We believe that this opens a window of opportunity for GAMMA-MRI using the snapshot image acquisition method that has been discussed within the consortium if whole brain image acquisition can be repeated with a relatively high frequency (every second or so, or ideally faster than that). Under the assumption that this approach works, it is conceivable, probably with continuous delivery of mXe, that GAMMA-MRI could capture some of the neuronal mechanisms occurring within period 1 and offer unprecedented spatial and maybe

temporal resolution when it comes to functional brain imaging. The road to this experimental result is obviously long but it is an opportunity to consider, that could additionally distinguish GAMMA-MRI from other functional brain imaging modalities.

Note that our model retains a similar quality of qualitative and quantitative predictions in rodents. While we focussed here on humans, the same model – with mostly the same dynamics and mostly equal internal time constants – works equally well in predicting the behaviour of key metabolites in rodents. There is thus no reason to think that the results introduced here do not generalise to the animal experimental models we will be using initially within GAMMA-MRI.

2.5. Looking ahead to *in vivo* experiments

2.5.1. Modelling the detailed dynamics of xenon

Task 5.1 continues in the final reporting period of the project until Sept. 2024. In anticipation of the *in vivo* experiments that will take place next year, we are now expanding our modelling effort to add the explicit dynamics of xenon to our model of neuron-astrocyte-vasculature metabolic interactions. To this end, we have started incorporating the model of Rao *et al.* into our formalism (*Magn. Reson. Med.* 85, 2021).

Because xenon is inert and passively transported from the vasculature to the parenchyma, there is however little indication that it can lead to meaningful biological effects at the timescales we hope to detect it. We thus anticipate that not a lot of additional information will come from this effort. The dynamics of xenon will be entirely determined by its influx into the circulation, and by its passive diffusion in and out of the brain tissue. Thus, its tissular and vascular dynamics will be mostly determined by cerebral blood flow and neurovascular coupling on one hand, and by the dynamics of inhalation on the other hand. Note additionally that the uptake of inhaled hyperpolarized (^{129}Xe) xenon in brain tissue is calculated to be ~1-2% only (Shepelytskyi *et al.*, *Magn. Reson. Med.* 88, 2022), yielding its highest signal-to-noise ratio in *in vivo* experiments about 40 s after inhalation (Rao *et al.*, *Radiology* 286, 2018). Moreover, Ostwald coefficients have been determined *in vivo* in the dog brain for ^{133}Xe as 0.189 ± 007, 0.26 ± 0.01 and 0.177 ± 0.06 for the cerebral cortex, cortical white matter and cortical grey matter, respectively (Chen *et al.*, *J. App. Physiol.* 49, 1980).

Using this augmented formalism, we do plan on modelling next year different types of inhalation dynamics. However, it is unclear that this will come into play in the first *in vivo* experiments within GAMMA-MRI, as these experiments already represent a significant challenge on their own. However, these results will be used on the long-term to fine tune future experimental protocols.

2.5.2. Modelling pathophysiology (stroke)

Finally, in view of supporting applications of GAMMA-MRI to stroke, we have implemented in our modelling framework simulations of transient ischemic stroke to assess how the neuro-astrocytic-vascular complex is affected. Our modelling framework allows to readily simulate this by a reduction of baseline cerebral blood flow in absence of stimulation (although this would also be possible) (see Figure 4).

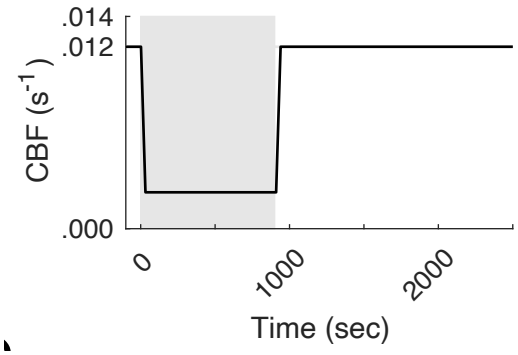

Figure 4. Simulating a transient ischemic stroke in the human version of our model of brain energy metabolism as an 80% reduction of incoming blood flow.

In general, it is our considered view that pathophysiology cannot be appropriately modelled using computational neuroscience tools today, because of the large number of slow cellular processes that are induced by any pathological modification of the brain tissue and not accounted for in such models. We believe however that an ischemic stroke, particularly if it is transient, is the exception to this rule, as this type of ischemia has a punctual temporal and spatial origin, which can be easily modelled, and whose short-term effects can – to an extent – also be accounted for in a computational model.

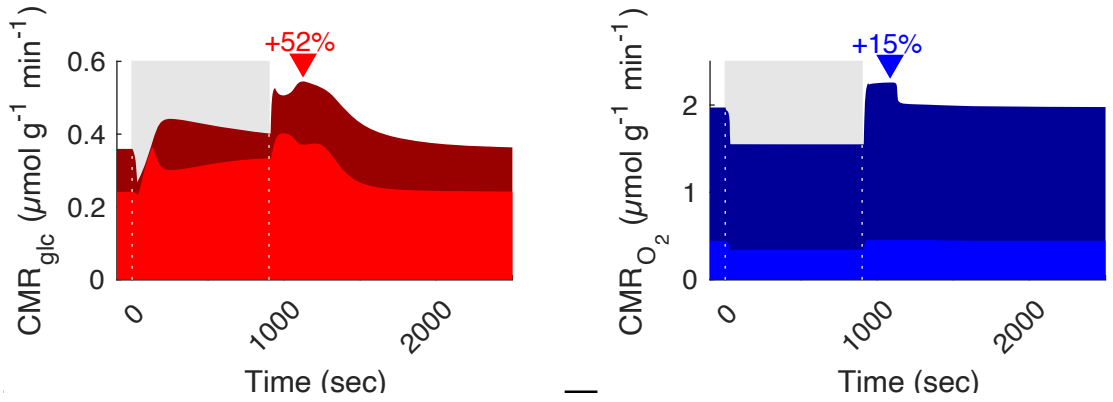

Figure 5. Dynamic of baseline glucose and oxygen consumption in our model of transient ischemic stroke.

Our simulations show rapid and significant changes in the baseline consumption of oxygen and glucose (Figure 5 above), both at the onset of the transient ischemic attack (grey box), and after restoration of normal cerebral blood flow (at time = 1000 s in these simulations). The balance of glucose consumption between the neuronal (dark red) and glial (bright red) compartments is also significantly affected throughout. Interestingly, the transient stroke also leads to an upset of the balance between baseline oxygen and glucose consumptions, with a stark reduction of the oxygen consumption (Figure 5 right). This naturally leads to an overproduction of lactate in the ischemic region, a well-documented clinical fact, which again was not *a priori* built in our model. This can be observed in simulations of the tissular lactate dynamics in Figure 6 below. Finally, this can also be confirmed from the evolution of the oxygen-glucose index, which is a direct ratio of the results in Figure 5 above (Figure 7).

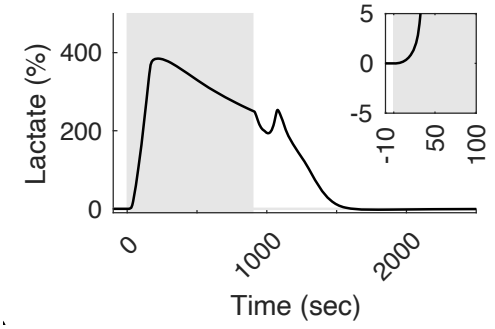

Figure 6. Evolution of tissular lactate in our model of a transient ischemic stroke.

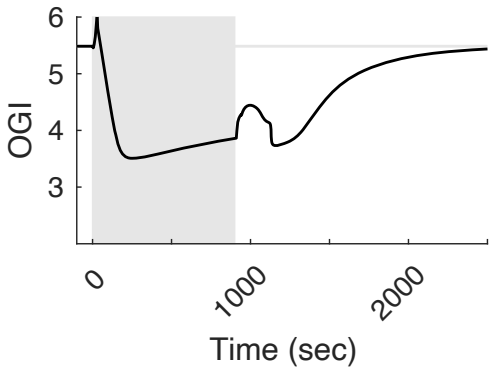

Figure 7. Evolution of the oxygen-glucose index in our model of a transient ischemic stroke.

Going forward into the last reporting period of the GAMMA-MRI project, we will be merging the efforts from this approach with the efforts described in subsection 2.5.1 to complete a revised model of brain energy metabolism in physiology and pathophysiology (specifically stroke, as discussed above), including the full dynamics of inhaled xenon. We expect that going forward and looking beyond the current GAMMA-MRI project, this revised model can be used to fine-tune the experimental protocol used for *in vivo* imaging experiments in healthy animals, and in experimental models of medial cerebral artery occlusion.

3. Conclusions

In this report, we described our efforts towards the development and comprehensive analysis of a computational framework supporting the *in vivo* imaging experiments that will be performed next year, and presumably in the future in future iterations of the GAMMA-MRI consortium. We reported our efforts at using CSP to investigate the detailed behaviour of the complex network of neurometabolic reactions and identified a possible technological point of interest for the future development of the GAMMA-MRI imaging modality. We also reported on our efforts to complement our existing computational framework by adding the detailed and most probably passive dynamics of the inert gas xenon, and on separate but complementary efforts to model stroke within that framework.

As discussed above, we will now proceed in the last reporting period to merge these approaches and produce the simulations that could allow us improving on future *in vivo* experiments.

Annex 1: Parameters and equations of the original model

Table 1. Governing equations.

Variable	Value	Equation	
Intracellular sodium	8/15 mM *	$\frac{d}{dt}Na_x^+ = J^x_{leak,Na} - 3\,J^x_{pump} + J^x_{stim}(t)$	* (A.1)
Neuronal glucose	1.20 mM	$\frac{d}{dt}GLC_n = J^{en}_{GLC} - J^n_{HKPFK}$	(A.2)
Astrocytic glucose	1.19 mM	$\frac{d}{dt}GLC_g = J^{eg}_{GLC} + J^{eg}_{GLC} - J^g_{HKPFK}$	(A.3)
Glyceraldehyde-3-phosphate	0.0046 mM	$\frac{d}{dt}GAP_x = 2\,J^x_{HKPFK} - J^x_{PGK}$	(A.4)
Phosphoenolpyruvate	0.015 mM	$\frac{d}{dt}PEP_x = J^x_{PGK} - J^x_{PK}$	(A.5)
Pyruvate	0.17 mM	$\frac{d}{dt}PYR_x = J^x_{PK} - J^x_{LDH} - J^x_{mito,in}$	(A.6)
Neuronal lactate	0.6 mM	$\frac{d}{dt}LAC_n = J^n_{LDH} - J^{ne}_{LAC}$	(A.7)
Astrocytic lactate	0.6 mM	$\frac{d}{dt}LAC_g = J^g_{LDH} - J^{ge}_{LAC} - J^{gc}_{LAC}$	(A.8)
Cytosolic NADH †	0.006/0.1 mM	$\frac{d}{dt}NADH^{cyto}_x = (1-\xi)^{-1}\,(J^x_{PGK} - J^x_{LDH} - J^x_{shuttle})$	(A.9)
Mitchondrial NADH †	0.12 mM	$\frac{d}{dt}NADH^{mito}_x = \xi^{-1}\,\left(4\,J^x_{mito,in} - J^x_{mito,out} + J^x_{shuttle}\right)$	(A.10)
Neuronal ATP ‡	2.2 mM	$\frac{d}{dt}ATP_n = (-2\,J^n_{HKPFK} + J^n_{PGK} + J^n_{PK} - J^n_{ATPases} - J^n_{pump} + 3.6\,J^n_{mito,out} + J^n_{CK})\,\left(1 - \frac{d\,AMP_n}{dATP_n}\right)^{-1}$	(A.11)
Astrocytic ATP ‡	2.2 mM	$\frac{d}{dt}ATP_g = (-2\,J^g_{HKPFK} + J^g_{PGK} + J^g_{PK} - J^g_{ATPases} - 7/4\,J^g_{pump} + 3/4\,J^g_{pump,0} + 3.6\,J^g_{mito,out} + J^g_{CK})\,\left(1 - \frac{d\,AMP_g}{dATP_g}\right)^{-1}$	(A.12)
Phosphocreatine	4.9 mM	$\frac{d}{dt}PCr_x = -J^x_{CK}$	(A.13)
Neuronal oxygen	0.028 mM	$\frac{d}{dt}O_{2n} = J^{cn}_{O_2m} - 0.6\,J^n_{mito,out}$	(A.14)
Astrocytic oxygen	0.028 mM	$\frac{d}{dt}O_{2g} = J^{cg}_{O_2m} - 0.6\,J^g_{mito,out}$	(A.15)
Capillary oxygen	7.0 mM	$\frac{d}{dt}O_{2c} = J^c_{O_2} - 1/r_{cn}\,J^{cn}_{O_2m} - 1/r_{cg}\,J^{cg}_{O_2m}$	(A.16)
Capillary glucose	4.5 mM	$\frac{d}{dt}GLC_c = J^c_{GLC} - 1/r_{ce}\,J^{ce}_{GLC} - 1/r_{cg}\,J^{cg}_{GLC}$	(A.17)
Capillary lactate	0.55 mM	$\frac{d}{dt}LAC_c = J^c_{LAC} + 1/r_{ce}\,J^{ec}_{LAC} + 1/r_{cg}\,J^{gc}_{LAC}$	(A.18)
Venous volume	0.02	$\frac{d}{dt}V_v = F_{in}(t) - F_{out}$	* (A.19)
Deoxyhemoglobin	0.058 mM	$\frac{d}{dt}dHb = F_{in}(t)\,(O_{2a} - O_{2\bar{c}}) - F_{out}\,\frac{dHb}{V_v}$	* (A.20)
Extracellular glucose	2.48 mM	$\frac{d}{dt}GLC_e = J^{ce}_{GLC} - 1/r_{eg}\,J^{eg}_{GLC} - 1/r_{en}\,J^{en}_{GLC}$	(A.21)
Extracellular lactate	0.6 mM	$\frac{d}{dt}LAC_e = 1/r_{en}\,J^{ne}_{LAC} + 1/r_{eg}\,J^{ge}_{LAC} - J^{ec}_{LAC}$	(A.22)
Neuronal membrane voltage	-73 mV	$\frac{d}{dt}\psi_n = C_m^{-1}\,[-I_L - I_{Na} - I_K - I_{Ca} - I_{mAHP} - I_{pump} + I_{syn}(t)]$	* (A.23)
h gating variable	0.99	$\frac{d}{dt}h = \frac{\phi_h}{\tau_h}\,(h_\infty - h)$	(A.24)
n gating variable	0.02	$\frac{d}{dt}n = \frac{\phi_n}{\tau_n}\,(n_\infty - n)$	(A.25)
Neuronal calcium	$5\,10^{-5}$ mM	$\frac{d}{dt}Ca^{2+} = -\frac{S_m V_n}{F}\,I_{Ca} - 1/\tau_{Ca}\,(Ca^{2+} - Ca_0^{2+})$	(A.26)

* When two values are indicated, the first one corresponds to the neuronal compartment and the second one to the astrocytic compartment.

† NADH stands for nicotinamide adenine dinucleotide.

‡ ATP stands for adenosine triphosphate.

Table 2. Rates, transports and currents.

Reaction, transport or current	Equation	
Sodium leak	$\mathrm{J}^{\mathrm{x}}_{\mathrm{leak,Na}} = \frac{\mathrm{S_m V_x}}{F}\, g^{\mathrm{x}}_{\mathrm{Na}} \left[\frac{RT}{F}\, \log\left(\mathrm{Na}^+_{\mathrm{e}}/\mathrm{Na}^+_{\mathrm{x}}\right) - \psi_{\mathrm{x}}\right]$	**(A.27)**
Na,K-ATPase	$\mathrm{J}^{\mathrm{x}}_{\mathrm{pump}} = \mathrm{S_m V_x}\, k^{\mathrm{x}}_{\mathrm{pump}}\, \mathrm{ATP_x}\, \mathrm{Na}^+_{\mathrm{x}} \left(1 + \frac{\mathrm{ATP_x}}{K_{\mathrm{m,pump}}}\right)^{-1}$	**(A.28)**
Glucose transport	$\mathrm{J}^{\mathrm{xy}}_{\mathrm{GLC}} = T^{\mathrm{xy}}_{\mathrm{max,GLC}} \left[\frac{\mathrm{GLC_x}}{\mathrm{GLC_x} + K^{\mathrm{xy}}_{\mathrm{t,GLC}}} - \frac{\mathrm{GLC_y}}{\mathrm{GLC_y} + K^{\mathrm{xy}}_{\mathrm{t,GLC}}}\right]$	**(A.29)**
Hexokinase-phosphofructokinase	$\mathrm{J}^{\mathrm{x}}_{\mathrm{HKPFK}} = k^{\mathrm{x}}_{\mathrm{HKPFK}}\, \mathrm{ATP_x}\, \frac{\mathrm{GLC_x}}{\mathrm{GLC_x} + K_g} \left[1 + \left(\frac{\mathrm{ATP_x}}{K_{\mathrm{I,ATP}}}\right)^{nH}\right]^{-1}$	**(A.30)**
Phosphoglycerate kinase	$\mathrm{J}^{\mathrm{x}}_{\mathrm{PGK}} = k^{x}_{\mathrm{PGK}}\, \mathrm{GAP_x}\, \mathrm{ADP_x}\, (N - \mathrm{NADH}^{\mathrm{cyto}}_{\mathrm{x}})/\mathrm{NADH}^{\mathrm{cyto}}_{\mathrm{x}}$	**(A.31)**
Pyruvate kinase	$\mathrm{J}^{\mathrm{x}}_{\mathrm{PK}} = k^{\mathrm{x}}_{\mathrm{PK}}\, \mathrm{PEP_x}\, \mathrm{ADP_x}$	**(A.32)**
Lactate dehydrogenase	$\mathrm{J}^{\mathrm{x}}_{\mathrm{LDH}} = k^{\mathrm{x}+}_{\mathrm{LDH}}\, \mathrm{PYR_x}\, \mathrm{NADH}^{\mathrm{cyto}}_{\mathrm{x}} - k^{\mathrm{x}-}_{\mathrm{LDH}}\, \mathrm{LAC_x}\, \left(N - \mathrm{NADH}^{\mathrm{cyto}}_{\mathrm{x}}\right)$	**(A.33)**
Lactate transport	$\mathrm{J}^{\mathrm{xy}}_{\mathrm{LAC}} = T^{\mathrm{xy}}_{\mathrm{max,LAC}} \left[\frac{\mathrm{LAC_x}}{\mathrm{LAC_x} + K^{\mathrm{xy}}_{\mathrm{t,LAC}}} - \frac{\mathrm{LAC_y}}{\mathrm{LAC_y} + K^{\mathrm{xy}}_{\mathrm{t,LAC}}}\right]$	**(A.34)**
TCA cycle	$\mathrm{J}^{\mathrm{x}}_{\mathrm{mito,in}} = V^{\mathrm{x}}_{\mathrm{max,in}}\, \frac{\mathrm{PYR_x}}{\mathrm{PYR_x} + K^{\mathrm{mito}}_{\mathrm{m}}}\, \frac{N - \mathrm{NADH}^{\mathrm{mito}}_{\mathrm{x}}}{N - \mathrm{NADH}^{\mathrm{mito}}_{\mathrm{x}} + K^{\mathrm{x}}_{\mathrm{m,NAD}}}$	**(A.35)**
Electron transport chain	$\mathrm{J}^{\mathrm{x}}_{\mathrm{mito,out}} = V^{\mathrm{x}}_{\mathrm{max,out}}\, \frac{\mathrm{O_{2x}}}{\mathrm{O_{2x}} + \mathrm{K}^{\mathrm{mito}}_{\mathrm{O_2}}}\, \frac{\mathrm{ADP_x}}{\mathrm{ADP_x} + K^{\mathrm{x}}_{\mathrm{m,ADP}}}\, \frac{\mathrm{NADH}^{\mathrm{mito}}_{\mathrm{x}}}{\mathrm{NADH}^{\mathrm{mito}}_{\mathrm{x}} + K^{\mathrm{x}}_{\mathrm{m,NADH}}}$	**(A.36)**
NADH shuttles	$\mathrm{J}^{\mathrm{x}}_{\mathrm{shuttle}} = T^{\mathrm{x}}_{\mathrm{NADH}}\, \frac{R^-_{\mathrm{x}}}{M^{\mathrm{cyto}}_{\mathrm{x}} + R^-_{\mathrm{x}}}\, \frac{R^+_{\mathrm{x}}}{M^{\mathrm{mito}}_{\mathrm{x}} + R^+_{\mathrm{x}}}$	†**(A.37)**
Creatine kinase	$\mathrm{J}^{\mathrm{x}}_{\mathrm{CK}} = k^{\mathrm{x}+}_{\mathrm{CK}}\, \mathrm{PCr_x}\, \mathrm{ADP_x} - k^{\mathrm{x}-}_{\mathrm{CK}}\, (C - \mathrm{PCr_x})\, \mathrm{ATP_x}$	**(A.38)**
Oxygen exchange between capillary and cells	$\mathrm{J}^{\mathrm{cx}}_{\mathrm{O_2 m}} = \frac{PS_{\mathrm{cap}}}{\mathrm{V_x}} \left(K_{\mathrm{O_2}} \left(\frac{Hb.OP}{\mathrm{O_{2c}}} - 1\right)^{-1/nh} - \mathrm{O_{2n}}\right)$	**(A.39)**
Blood flow contribution to capillary oxygen	$\mathrm{J}^{\mathrm{c}}_{\mathrm{O_2}} = \frac{2\, F_{\mathrm{in}}(t)}{V_{\mathrm{cap}}}\, (\mathrm{O_{2a}} - \mathrm{O_{2c}})$	*†**(A.40)**
Blood flow contribution to capillary glucose	$\mathrm{J}^{\mathrm{c}}_{\mathrm{GLC}} = \frac{2\, F_{\mathrm{in}}(t)}{V_{\mathrm{cap}}}\, (\mathrm{GLC_a} - \mathrm{GLC_c})$	*†**(A.41)**
Blood flow contribution to capillary lactate	$\mathrm{J}^{\mathrm{c}}_{\mathrm{LAC}} = \frac{2\, F_{\mathrm{in}}(t)}{V_{\mathrm{cap}}}\, (\mathrm{LAC_a} - \mathrm{LAC_c})$	*†**(A.42)**
Oxygen concentration at the end of the capillary	$\mathrm{O_{2\bar{c}}} = 2\, \mathrm{O_{2c}} - \mathrm{O_{2a}}$	**(A.43)**
Leak current	$I_L = g_L\, (\psi_{\mathrm{n}} - E_L)$	**(A.44)**
Voltage-dependent sodium current	$I_{\mathrm{Na}} = g_{\mathrm{Na}}\, m^3_\infty\, h \left(\psi_{\mathrm{n}} - \frac{RT}{F}\, \log(\mathrm{Na}^+_{\mathrm{e}}/\mathrm{Na}^+_{\mathrm{n}})\right)$	‡**(A.45)**
Potassium rectifier current	$I_{\mathrm{K}} = g_{\mathrm{K}}\, n^4\, (\psi_{\mathrm{n}} - E_{\mathrm{K}})$	‡**(A.46)**
Calcium current	$I_{\mathrm{Ca}} = g_{\mathrm{Ca}}\, m^2_{\mathrm{Ca}}\, (\psi_{\mathrm{n}} - E_{\mathrm{Ca}})$	‡**(A.47)**
Calcium-dependent potassium current	$I_{\mathrm{mAHP}} = g_{\mathrm{mAHP}}\, \frac{\mathrm{Ca}^{2+}}{\mathrm{Ca}^{2+} + K_D}\, (\psi_{\mathrm{n}} - E_{\mathrm{K}})$	**(A.48)**
Na,K-ATPase current	$I_{\mathrm{pump}} = F\, k^{\mathrm{n}}_{\mathrm{pump}}\, \mathrm{ATP_n}\, (\mathrm{Na}^+_{\mathrm{n}} - \mathrm{Na}^+_{\mathrm{n0}}) \left(1 + \frac{\mathrm{ATP_x}}{K_{\mathrm{m,pump}}}\right)^{-1}$	**(A.49)**
Flow out of the venous balloon	$F_{\mathrm{out}} = F_0 \left[\left(\frac{\mathrm{V_v}}{\mathrm{V_{v0}}}\right)^{1/\alpha_{\mathrm{v}}} + \frac{\tau_{\mathrm{v}}}{\mathrm{V_{v0}}} \left(\frac{\mathrm{V_v}}{\mathrm{V_{v0}}}\right)^{-1/2} \frac{\mathrm{d\, V_v}}{dt}\right]$	**(A.50)**

† **With** $R^-_{\mathrm{x}} = \mathrm{NADH}^{\mathrm{cyto}}_{\mathrm{x}}/(N - \mathrm{NADH}^{\mathrm{cyto}}_{\mathrm{x}})$ **and** $R^+_{\mathrm{x}} = (N - \mathrm{NADH}^{\mathrm{mito}}_{\mathrm{x}})/\mathrm{NADH}^{\mathrm{mito}}_{\mathrm{x}}$.

‡ **Further equations in the Hodgkin-Huxley model are** $\alpha_m = -0.1\,(\psi_{\mathrm{n}} + 33)/(\exp[-0.1\,\{\psi_{\mathrm{n}} + 33\}] - 1)$, $\beta_m = 4\, \exp[-\{\psi_{\mathrm{n}} + 58\}/12]$, $\alpha_h = 0.07\, \exp[-\{\psi_{\mathrm{n}} + 50\}/10]$, $\beta_h = 1/(\exp[-0.1\,\{\psi_{\mathrm{n}} + 20\}] + 1)$, $\alpha_n = -0.01\,(\psi_{\mathrm{n}} + 34)/(\exp[-0.1\,\{\psi_{\mathrm{n}} + 34\}] - 1)$, $\beta_n = 0.125\, \exp[-\{\psi_{\mathrm{n}} + 44\}/25]$, $m_\infty = \alpha_m\, (\alpha_m + \beta_m)^{-1}$, $n_\infty = \alpha_n\, (\alpha_n + \beta_n)^{-1}$, $h_\infty = \alpha_h\, (\alpha_h + \beta_h)^{-1}$, $\tau_n = 10^{-3}\, (\alpha_n + \beta_n)^{-1}$, $\tau_h = 10^{-3}\, (\alpha_h + \beta_h)^{-1}$, $m_{\mathrm{Ca}} = 1/(1 + \exp[-\{\psi_{\mathrm{n}} + 20\}/9])$ **and** $E_L = (g^{\mathrm{pas}}_K + g^{\mathrm{n}}_{\mathrm{Na}})^{-1} \left[g^{\mathrm{pas}}_K\, E_{\mathrm{K}} + g^{\mathrm{n}}_{\mathrm{Na}}\, \frac{RT}{F}\, \log(\mathrm{Na}^+_{\mathrm{e}}/\mathrm{Na}^+_{\mathrm{n}})\right]$.

Table 3. Parameters.

Fixed parameters	
Volume fractions:	$\mathrm{V_e} = 0.2$, $\mathrm{V_{cap}} = 0.0055$, $\mathrm{V_g} = 0.25$, $\mathrm{V_n} = 0.45$, $\xi = 0.07$ (mitochondrial volume fraction $= \mathrm{V_{mito}/V_{cell}}$), $r_{\mathrm{en}} = \mathrm{V_e/V_n}$, $r_{\mathrm{eg}} = \mathrm{V_e/V_g}$, $r_{\mathrm{ce}} = \mathrm{V_{cap}/V_e}$, $r_{\mathrm{cn}} = \mathrm{V_{cap}/V_n}$, $r_{\mathrm{cg}} = \mathrm{V_{cap}/V_g}$
Surface to volume ratios:	$\mathrm{S_mV_n} = 2.5\,10^4$ cm^{-1}, $\mathrm{S_mV_g} = 2.5\,10^4$ cm^{-1}
Physical constants:	$R = 8.31451$ J mol^{-1} K^{-1}, $F = 9.64853\,10^4$ C mol^{-1}, $RT/F = 26.73$ mV (corresponds to body temperature), $\psi_{\mathrm{g}} = -70$ mV, $\mathrm{Na_e^+} = 150$ mM
Glucose exchange affinities:	$K^{\mathrm{en}}_{\mathrm{t,GLC}} = 8$, $K^{\mathrm{eg}}_{\mathrm{t,GLC}} = 8$, $K^{\mathrm{cg}}_{\mathrm{t,GLC}} = 8$, $K^{\mathrm{ce}}_{\mathrm{t,GLC}} = 8$ mM
Lactate exchange affinities:	$K^{\mathrm{en}}_{\mathrm{t,LAC}} = 0.74$, $K^{\mathrm{ge}}_{\mathrm{t,LAC}} = 3.5$, $K^{\mathrm{gc}}_{\mathrm{t,LAC}} = 1.0$, $K^{\mathrm{ec}}_{\mathrm{t,LAC}} = 1.0$ mM
Hexokinase-phosphofructokinase system:	$K_{\mathrm{I,ATP}} = 1$ mM, $nH = 4$, $K_g = 0.05$ mM
Oxygen exchange constants:	$K_{\mathrm{O_2}} = 0.0361$ mM, $Hb.OP = 8.6$ mM, $nh = 2.73$
Electron transport chain:	$K^{\mathrm{mito}}_{\mathrm{O_2}} = 0.001$ mM
Hodgkin-Huxley parameters:	$C_m = 10^{-3}$ mF cm^{-2}, $g_L = 0.02$, $g_{\mathrm{Na}} = 40$, $g_{\mathrm{K}} = 18$, $g_{\mathrm{Ca}} = 0.02$, $g_{\mathrm{mAHP}} = 6.5$ mS cm^{-2}, $K_D = 30\,10^{-3}$ mM, $\tau_{\mathrm{Ca}} = 150\,10^{-3}$ s, $\mathrm{Ca_0^{2+}} = 0.5\,10^{-4}$ mM, $E_{\mathrm{K}} = -80$, $E_{\mathrm{Ca}} = 120$ mV, $\phi_h = \phi_n = 4$
Venous balloon:	$\tau_{\mathrm{v}} = 35$ s, $\alpha_{\mathrm{v}} = 0.5$
Blood flow contribution to capillary glucose and oxygen:	$\mathrm{O_{2a}} = 8.35$, $\mathrm{GLC_a} = 4.75$ mM
Na,K-ATPase and sodium leak:	$g^{\mathrm{n}}_{\mathrm{Na}} = 0.0136$, $g^{\mathrm{g}}_{\mathrm{Na}} = 0.0061$, $g^{\mathrm{pas}}_{\mathrm{K}} = 0.2035$ mS cm^{-2}, $k^{\mathrm{n}}_{\mathrm{pump}} = 2.2\,10^{-6}$, $k^{\mathrm{g}}_{\mathrm{pump}} = 4.5\,10^{-7}$ cm mM^{-1} s^{-1}, $J^{\mathrm{g}}_{\mathrm{pump},0} = 0.0687$ mM s^{-1}, $K_{\mathrm{m,pump}} = 0.5$ mM
Total creatine plus phosphocreatine concentration:	$C = 10$ mM
Total nicotinamide adenine dinucleotide concentration:	$N = 0.212$ mM
TCA cycle:	$K^{\mathrm{mito}}_{\mathrm{m}} = 0.04$ mM
Optimized parameters	
Lactate dehydrogenase:	$k^{\mathrm{n+}}_{\mathrm{LDH}} = 72.3$, $k^{\mathrm{g+}}_{\mathrm{LDH}} = 1.59$ L mmol^{-1} s^{-1}
NADH shuttles:	$M^{\mathrm{cyto}}_{\mathrm{n}} = 4.9\,10^{-8}$, $M^{\mathrm{cyto}}_{\mathrm{g}} = 2.5\,10^{-4}$, $M^{\mathrm{mito}}_{\mathrm{n}} = 3.93\,10^5$, $M^{\mathrm{mito}}_{\mathrm{g}} = 1.06\,10^4$
Electron transport chain:	$K^{\mathrm{n}}_{\mathrm{m,ADP}} = 3.41\,10^{-3}$, $K^{\mathrm{g}}_{\mathrm{m,ADP}} = 0.483\,10^{-3}$, $K^{\mathrm{n}}_{\mathrm{m,NADH}} = 4.44\,10^{-2}$, $K^{\mathrm{g}}_{\mathrm{m,NADH}} = 2.69\,10^{-2}$ mM
Creatine kinase:	$k^{\mathrm{n+}}_{\mathrm{CK}} = 0.0433$, $k^{\mathrm{g+}}_{\mathrm{CK}} = 0.00135$ mM^{-1} s^{-1}
TCA cycle:	$K^{\mathrm{n}}_{\mathrm{m,NAD}} = 0.409$, $K^{\mathrm{g}}_{\mathrm{m,NAD}} = 40.3$ mM
Constrained parameters	
Glucose exchanges constants:	$T^{\mathrm{en}}_{\mathrm{max,GLC}} = 0.041$, $T^{\mathrm{ce}}_{\mathrm{max,GLC}} = 0.239$, $T^{\mathrm{eg}}_{\mathrm{max,GLC}} = 0.147$, $T^{\mathrm{cg}}_{\mathrm{max,GLC}} = 0.0016$ mM s^{-1}
Lactate exchanges constants:	$T^{\mathrm{gc}}_{\mathrm{max,LAC}} = 0.00243$, $T^{\mathrm{ne}}_{\mathrm{max,LAC}} = 24.3$, $T^{\mathrm{ge}}_{\mathrm{max,LAC}} = 106.1$, $T^{\mathrm{ec}}_{\mathrm{max,LAC}} = 0.25$ mM s^{-1}
Hexokinase-phosphofructokinase system:	$k^{\mathrm{n}}_{\mathrm{HKPFK}} = 0.0504$, $k^{\mathrm{g}}_{\mathrm{HKPFK}} = 0.185$ s^{-1}
Lactate dehydrogenase:	$k^{\mathrm{n-}}_{\mathrm{LDH}} = 0.72$, $k^{\mathrm{g-}}_{\mathrm{LDH}} = 0.071$ L mmol^{-1} s^{-1}
Oxygen exchange constants:	$\frac{PS_{\mathrm{cap}}}{\mathrm{V_n}} = 1.66$, $\frac{PS_{\mathrm{cap}}}{\mathrm{V_g}} = 0.87$ s^{-1}
Electron transport chain:	$V^{\mathrm{n}}_{\mathrm{max,out}} = 0.164$, $V^{\mathrm{g}}_{\mathrm{max,out}} = 0.064$ mM s^{-1}
TCA cycle:	$V^{\mathrm{n}}_{\mathrm{max,in}} = 0.1303$, $V^{\mathrm{g}}_{\mathrm{max,in}} = 5.7$ mM s^{-1}
Phosphoglycerate kinase:	$k^{\mathrm{n}}_{\mathrm{PGK}} = 3.97$, $k^{\mathrm{g}}_{\mathrm{PGK}} = 135.2$ mM^{-1} s^{-1}
Pyruvate kinase:	$k^{\mathrm{n}}_{\mathrm{PK}} = 36.7$, $k^{\mathrm{g}}_{\mathrm{PK}} = 401.7$ mM^{-1} s^{-1}
ATPases:	$J^{\mathrm{n}}_{\mathrm{ATPases}} = 0.1695$, $J^{\mathrm{g}}_{\mathrm{ATPases}} = 0.1404$ mM s^{-1}
Creatine kinase:	$k^{\mathrm{n-}}_{\mathrm{CK}} = 0.00028$, $k^{\mathrm{g-}}_{\mathrm{CK}} = 10^{-5}$ mM^{-1} s^{-1}
NADH shuttles:	$T^{\mathrm{n}}_{\mathrm{NADH}} = 10330$, $T^{\mathrm{g}}_{\mathrm{NADH}} = 150$ mM s^{-1}
Blood flow contribution to capillary lactate:	$\mathrm{LAC_a} = 0.506$ mM